



Research on the Microstructure Characteristic and Tensile Property of Laser-MIG Hybrid Welded Joint for 5A06 Aluminum Alloy

Yanqiu Zhao¹ · Xiaohong Zhan¹ · Qiyu Gao¹ · Shuai Chen¹ · Yue Kang¹

Received: 14 February 2019 / Accepted: 24 June 2019 / Published online: 10 July 2019
© The Korean Institute of Metals and Materials 2019

Abstract

Laser-metal inter gas (MIG) hybrid welding technique provides higher overall productivity over the traditional fusion welding processes for joining medium-thick aluminum alloy. In this paper, laser-MIG hybrid welding experiment was performed by the TruDisk 12003 Laser and KUKA robot. The second fusion line, the laser-dominated region and laser-MIG hybrid-dominated region were introduced to this study to discuss the microstructure distribution. A three-dimensional finite element model was established by MSC. Marc to study the thermal field distribution of laser-MIG hybrid welding process. It found that the temperature in the laser-MIG hybrid-dominated region was much higher than the laser-dominated region. The formation of the second fusion line in the welded joint is mainly owing to the different heat effect of laser-arc hybrid-dominated region and laser-dominated region. The crystalline size of equiaxed dendrite grains in the laser-MIG hybrid-dominated region is finer than the laser-dominated region. In addition, the tensile property was measured to dissect the failure mechanism of the laser-MIG hybrid welding joints. The element content in fractured surface at the position of dimple and pore wall were comprehensively analyzed. The element content of Mg and O in pore wall are higher than dimple. In the solidification process, the growth of equiaxed dendrite grains is in part hindered by the existence of coarse pores in the laser-MIG hybrid-dominated region.

Keywords Aluminum alloy · Dendrite · The second fusion line · Laser-MIG hybrid welding · Simulation

1 Introduction

It is universally recognized that aluminum alloys are extensively used in the aerospace and automotive thanks to the superior properties such as high specific strength and low density [1]. Al–Mg non-heat-treatment alloys are employed for pressure vessel structure which is required for corrosion resistance [2, 3]. Conventionally, the aluminum alloys were usually jointed through the metal inert gas (MIG) and tungsten inert gas (TIG) welding methods. The fusion penetration of these traditional MIG and TIG welding methods are relatively shallow owing to the poor efficiency and instable arc plasma [4]. On the other hand, the mechanical properties of the aluminum joints are critically ruined owing to the formation of new dendritic crystals [5–7]. Especially

for the aluminum alloy plate with a medium thickness at the range of 4.5–25 mm, the welding structures tend to be suffered from more challenges [8]. In order to improve the welding efficiency and obtain deeper penetration, laser beam welding is adopted due to its own high energy density [9, 10]. Unfortunately, aluminum alloy is a material with high reflectivity to the long-wavelength laser beam, which is not conducive to the absorption of laser heat source [11–13]. Aluminum alloy is difficult to be welded because of its own specific features i.e. high thermal conductivity, high thermal expansion, and the generation of oxide film Al_2O_3 [14]. Significantly, Al–Mg alloy is more difficult to be welded by laser beam owing to the high content of Mg element which is easily evaporated under the heat effect of laser beam. What's more, laser beam welding has insufficient gap bridging ability. With the strict requirement of the joint gap, individual laser beam welding is inappropriate to connect the medium-thick aluminum plate [15]. Besides, the weld quality gradually deteriorates with the increase of the plate thickness.

With the expectation of overcoming the drawbacks of single laser beam welding and traditional arc welding processes

✉ Xiaohong Zhan
xiaohongzhan_nuaa@126.com

¹ National Key Laboratory of Science and Technology on Helicopter Transmission, Nanjing University of Aeronautics and Astronautics, Nanjing 211106, China

for the medium-thick aluminum plates, laser-arc hybrid welding was developed in the late 1970s [16]. In laser-arc hybrid welding process, the laser beam plays a guiding role and stabilizes the arc voltage and current. The deeper penetration and better overall weld quality are achieved at a lower value of laser power [17–20]. Compared with the single laser beam and arc welding, laser-arc hybrid welding with two heat sources is a relatively progressive welding method which owns many advantages i.e. well bridging ability, excellent welding stability, and low residual stress [21, 22]. It has proved that the penetration of laser-arc hybrid welding is double comparing with TIG and five times of laser beam welding [23]. Moreover, the high arc voltage and short laser-arc distance would destabilize the welding process [24].

Recently, laser-MIG hybrid welding technology has been received considerable attention because of its high welding efficiency as well as excellent welding quality. Extensive studies of medium-thick aluminum alloy plates using laser-MIG hybrid welding have been carried out in different research fields, including welding parameters, mechanism property, microstructure and simulation. In the study of S Yan et al. [25], the softening behavior of laser-MIG welded joint for AA6005-T5 alloy was investigated. The results showed that the strength loss in the hybrid welded joint was mainly owing to the vaporization of Mg, Mn elements and the lower density of precipitates in the fusion zone. G. Gasalino et al. [26] studied the effects of the separate laser and arc powers on the weld properties for AA5754 aluminum alloy using hybrid welding. It was concluded that the high laser power was beneficial to the hybrid welding stability. Next year, for the same welding process and material, P. Leo et al. [27] researched the effect of power distribution on the welded joint. It was concluded that the better mechanical properties were obtained by a better power distribution. According to Bunaziv I et al. [11], it revealed the coarse porosity formation in fiber laser-MIG hybrid welding joint of 5 mm AA5083 and provided clarification to avoid it. Moradi M et al. detected the relationship of different welding parameters [28]. Besides, a three-dimensional finite element model of the laser-TIG hybrid welding was established [29]. The relationship of the molten pool characteristics and the weld percent porosity of laser-MIG hybrid welded joint for AA6082 aluminum alloy was investigated by Zhang et al. [30]. Besides, the porosity inhabitation mechanism and the effect of welding parameters on the porosity were discussed. Meng et al. [31] paid a lot of attention to the effect of groove parameters on the space constraint effect (SCE) of narrow gap laser-arc hybrid welding process. The SCE was obviously affected by the angle of groove and the width of rectangle groove. Cai et al. [32] concluded that the Ar–He shielding gas mixture improved the stability of keyhole. Although the results were promising for the application of

laser-MIG hybrid welding, challenges still existed i.e. the formation of porosity, softening behavior and hot crack. It is noteworthy that the dendrite and its effect on the mechanical properties in the welded joint was rarely researched.

For laser-MIG hybrid welding, the microstructure and tensile property of welded joint are seriously influenced by the welding condition and parameters. In the present work, the microstructure, temperature distribution and tensile property of the welded joints are analyzed. In microstructure, the second fusion zone, laser-dominated region and laser-MIG hybrid-dominated region are introduced to analyze the formation of dendrite grains with different crystalline size. Furthermore, the microstructure and temperature distribution from the simulation result are systematically researched to explain the formation of the two regions in the weld seam (WS).

2 Experiment

2.1 Equipments and Materials

The Laser-MIG hybrid welding equipments are shown in Fig. 1. The guide wire feeding and laser welding head are adjusted by the KUKA robot of KR60HA, whose kinematic accuracy is 0.5 mm. The laser beam is conducted

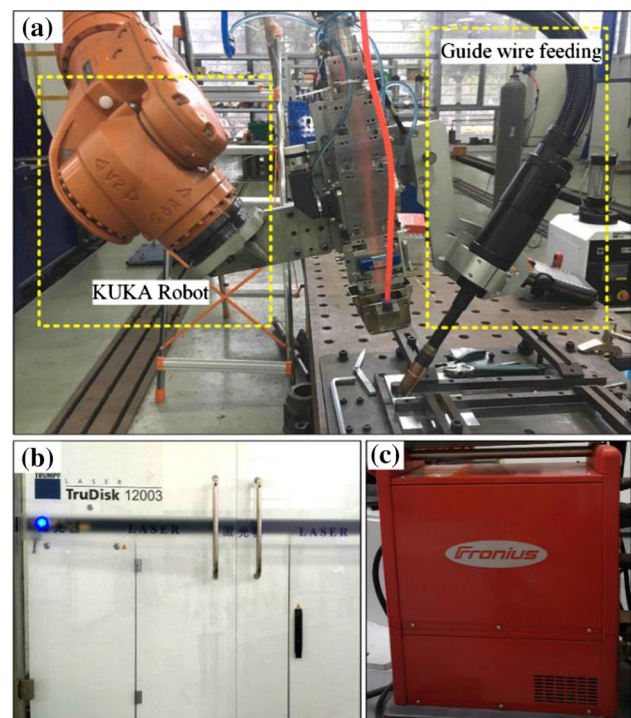


Fig. 1 Laser-MIG hybrid welding equipments. **a** KUKA robot of KR 60HA. **b** TruDisk 12003 Laser. **c** Fronius arc welding machine of TPS5000

Table 1 Parameters of TruDisk 12003 Laser

| | |
|--|------------|
| Wavelength | 1030 nm |
| Beam spot diameter | 45 μ m |
| Numerical aperture | 0.1 |
| Focal length of focusing mirror | 300 mm |
| Interface type of optical fiber output | QBH |
| Beam quality | 12 mm-mrad |

using TruDisk 12003 Laser, whose power is at the range of 320 W–12 kW. The detail technical parameters of the Laser are illustrated in Table 1. The laser welding head of Precitec YW52 matching the laser welding system is employed. Besides, Fronius arc welding machine of TPS5000 is used to control the welding parameters of electric arc.

The base metal (BM) used in this study is 5A06 aluminum alloy plate with the thickness of 6.9 mm. 5A06 aluminum alloy is mainly used in the spacecraft structure owing to its own high specific strength and excellent corrosion resistance. In this paper, the 5A06 aluminum alloy plates were machined to the dimension of 125 mm \times 50 mm \times 6.9 mm. With the expectation of the well penetration, the 30° Y-groove with a root face of 2 mm is adopted. The schematic diagram of laser-MIG hybrid welding with laser-arc distance of 3 mm is shown in Fig. 2a. The specific dimension of the groove shape and weldment are shown in Fig. 2b.

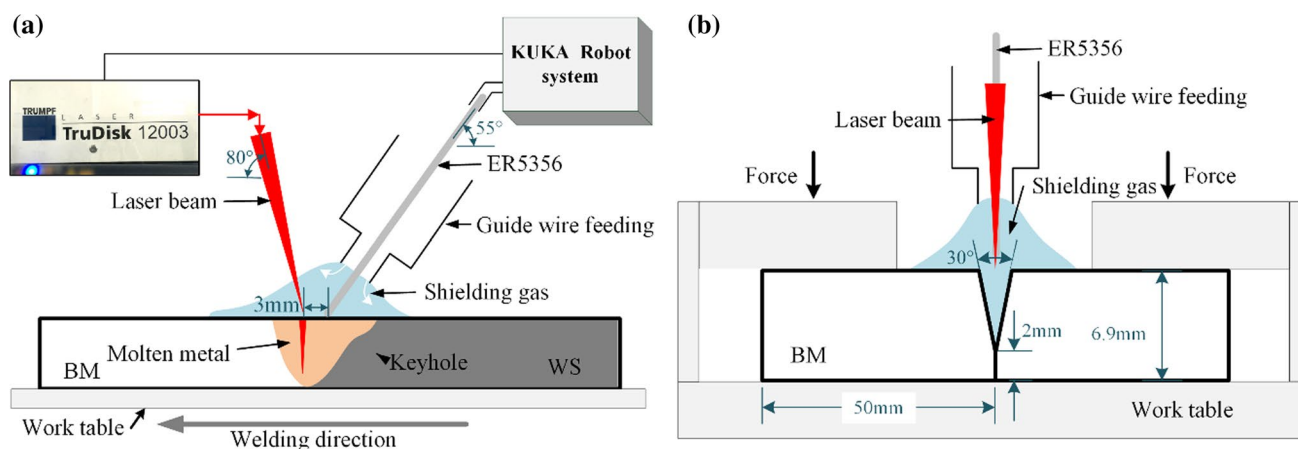
The ER5356 filler wire with a diameter of 1.2 mm is used, and the composition is similar to 5A06 aluminum alloy. The

chemical composition of 5A06 aluminum alloy and ER5356 filler wire are listed in Table 2.

2.2 Design of Experiment

The laser-arc distance has a critical influence on the coupling welding of laser beam and arc heat source. Because the lower laser-arc distance reduces the stability of the arc welding and the higher laser-arc distance weakens the coupling effect of laser beam and arc. In this paper, the laser-arc distance was designed into 3 mm. Along with the welding direction, the laser beam is in front of the MIG arc. The 5A06 aluminum alloy is firstly melted by the laser, thus the laser ahead of the MIG arc plays a leading role in this paper. The single laser beam welding process is shown as Fig. 3a. After 0.12–0.15 s, the electric arc works on the molten pool. The single MIG welding process is shown in Fig. 3b. Therefore, the bottom area of the welded joint is regard as single laser-dominated region, and the upper area is laser-arc hybrid-dominated region. At the same time, the second fusion line is formed between the both regions. The formation mechanism of laser-arc hybrid-dominated region is shown in Fig. 3c where the laser-arc hybrid-dominated region and laser-dominated region are separately marked.

The angle between the welding torch and the workpiece is 55°. The angle between the laser beam and the workpiece is 80°. The shielding gas flow is 15–20 L/min. The gap between the aluminum workpiece is approximately 0–0.2 mm. The specific welding parameters are picked from

**Fig. 2** The schematic diagram of laser-MIG hybrid welding. **a** Front view. **b** The side view**Table 2** Chemical composition of 5A06 and ER5356 (mass fraction, wt%)

| Element | Mg | Fe | Si | Zn | Ti | Mn | Cu | Be | Cr | Al |
|---------|-----|-----|------|-----|----------|----------|-----|-------|----------|---------|
| 5A06 | 6.8 | 0.4 | 0.4 | 0.2 | 0.1 | 0.8 | 0.1 | 0.005 | – | Balance |
| ER5356 | 5 | 0.4 | 0.25 | 0.1 | 0.06–0.2 | 0.05–0.2 | 0.1 | – | 0.05–0.2 | Balance |

plenty of preliminary experiments to ensure the well penetration. The final welding parameters utilized in this paper are as listed as Table 3. The well penetration weldment can be acquired with a laser power of 3.2–3.5KW for 6.9 mm 5A06 aluminum alloy. The welding velocity at a range of 1.2–1.5 m/min. The wire feed speed is determined by the welding velocity. The defocusing amount is at the range of 4–6 mm to reduce the intensity of laser power, decreasing the melting loss of alloying element.

2.3 Specimen Preparation

With the expectation of excellent weld quality, the proper surface treatment processing was employed prior to welding. The oxide film Al₂O₃ was smoothed by the angle grinder. Then, the acetone was used to wash the workpiece surface, wiping the oil and the grinded metallic powder. After laser-MIG hybrid welding experiment, the metallography samples of 10 mm × 20 mm × 6.9 mm were cut by wire cutting machine from weldment. Keller’s reagent was used to etch the samples which had been polished using standard metallographic techniques. The microstructure of 5A06 aluminum alloy welded joint was observed by MR-5000 optical microscope.

Besides, the weld samples for tensile testing were cut by wire cutting machine from the weldment. Tensile specimen was designed according to the requirement of GB/T 2651–2008, which is illustrated in Fig. 4. Tensile testing experiment was carried out using a tensile testing machine (UTM 5105). The tensile fracture was observed by SEM and the chemical composition distribution was tested by the EDS.

3 Model Theory

3.1 Mesh

Figure 5 presents the meshing result. The weldment component is divided into 49440 different hexahedron solid elements and has 55466 nodes. A coarse mesh is adopted in BM, where the effect of the hybrid heat sources is nearly neglected. Relatively, a subtle mesh is adopted near the WS, where the laser-MIG hybrid welding thermal process is mainly concerned. The minimum element of the WS is an irregular hexahedron with the shortest edge of 0.225 mm and the longest edge of 0.694 mm. The maximum element size away from the WS is approximately 2.08 mm × 3.54 mm × 1.73 mm.

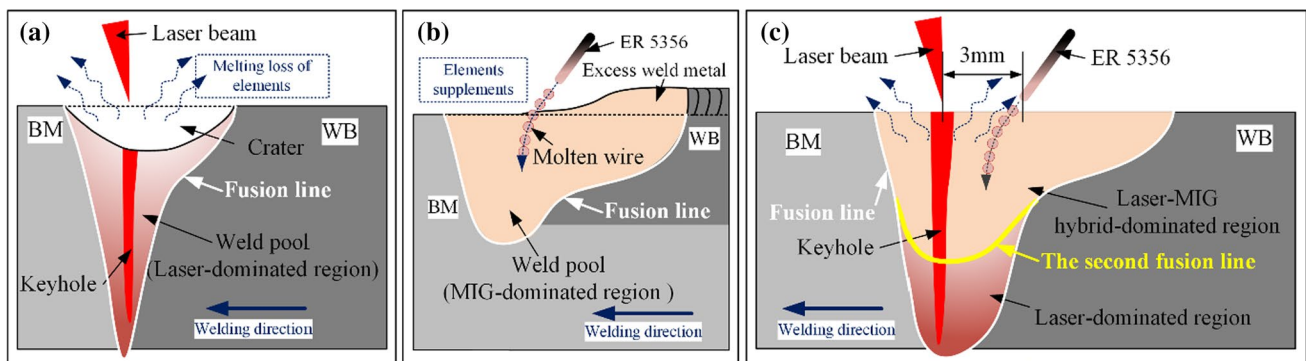


Fig. 3 The formation of laser-dominated region and laser-MIG hybrid-dominated region **a** Laser-dominated region in the laser welding process. **b** MIG-dominated region in the MIG welding process.

c Laser-dominated region and laser-MIG hybrid-dominated region in the laser-MIG hybrid welding

Table 3 The welding parameters of laser-MIG hybrid welding experiment with different groove shapes

| No. | Laser power (W) | Welding velocity (m/min) | Welding current (A) | Defocusing Amount (mm) | Gas flow rate (L/min) |
|-----|-----------------|--------------------------|---------------------|------------------------|-----------------------|
| 1 | 3500 | 1.5 | 137 | +4 | 15 |
| 2 | 3200 | 1.5 | 170 | +4 | 15 |
| 3 | 3200 | 1.2 | 170 | +4 | 20 |
| 4 | 3200 | 1.2 | 170 | +6 | 20 |
| 5 | 3200 | 1.3 | 170 | +4 | 20 |
| 6 | 3200 | 1.5 | 170 | +4 | 20 |

3.2 Heat Source Model and Heat Transfer Equation

Laser-MIG hybrid welding technology contains double heat source: laser beam and arc. The laser beam heat source is dominated in the hybrid welding process owing to the laser keyhole effect, while the arc heat source produces ellipsoid molten pool. Consequently, a single heat source is not accurate to simulate the hybrid thermal loading. In this paper, a compounded heat source model containing both the double-ellipsoid heat source and Gaussian rotator heat source is applied to characterize the hybrid welding. The double-ellipsoid heat source is shown in Fig. 6a and the Gaussian rotator heat source is shown in Fig. 6b.

The double-ellipsoid heat source contains two half-ellipsoid sections, which are formulated as follows:

$$q_1(x, y, z) = \begin{cases} q_r(x, y, z) = \frac{6\sqrt{3}f_r Q_1}{\pi^{\frac{2}{3}} a c_r h_1} \exp\left(-3\left(\left(\frac{x}{c_r}\right)^2 + \left(\frac{y}{a}\right)^2 + \left(\frac{z}{h_1}\right)^2\right)\right) & \text{if } x \in [-c_r, 0] \\ q_f(x, y, z) = \frac{6\sqrt{3}f_f Q_1}{\pi^{\frac{2}{3}} a c_f h_1} \exp\left(-3\left(\left(\frac{x}{c_f}\right)^2 + \left(\frac{y}{a}\right)^2 + \left(\frac{z}{h_1}\right)^2\right)\right) & \text{if } x \in [0, c_f] \end{cases} \quad (1)$$

where q_r is the heat flux density of the rear half ellipsoid and q_f is heat flux density of the front half ellipsoid. f_r and f_f are dimensionless factors expressed by Eqs. (2) and (3), $f_r + f_f = 2$. Q_1 is the heat input of arc power, c_r , c_f , a and h_1 are constant marked in Fig. 6a.

$$f_r = \frac{2}{1 + c_f/c_r} \quad (2)$$

$$f_f = \frac{2}{1 + c_r/c_f} \quad (3)$$

The Gaussian rotator heat source includes both Gauss face and body heat source [33]. The heat distribution equations of both Gauss face and body heat source are expressed by Eqs. (4) and (5).

$$q_s(x, y) = \frac{aQ_s}{\pi r_s^2} \exp\left(\frac{-a(x^2 + y^2)}{r_s^2}\right) \quad (4)$$

$$q_2(x, y, z) = \frac{9Q_v}{\pi r_s^2 H(1 - e^{-3})} \exp\left(\frac{-9(x^2 + y^2)}{\log \frac{H}{z}}\right) \quad (5)$$

where a is the heat flux concentration coefficient, Q_s and Q_v are separately the power of face and body heat source. r_s is

the effective radius and H is the depth as shown as Fig. 6b. The relationship between Q_s and Q_v is expressed by Eq. (6).

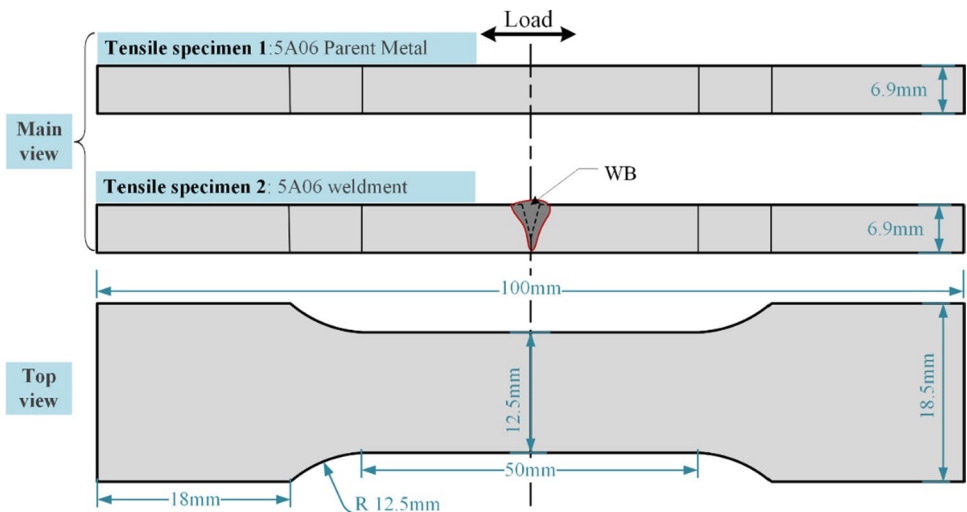
$$Q_2 \eta = Q_v + Q_s \quad (6)$$

where Q_2 is the heat input of laser beam power and η is the heat efficiency.

3.3 Thermal Property

The thermal properties of 5A06 aluminum alloy are not constant but change with the increasing temperature during welding process. The specific values of thermal conductivity and specific heat of different temperature are performed in Table 4 [34]. The melting point of 5A06 aluminum alloy is 560 °C.

Fig. 4 Dimension of tensile test samples



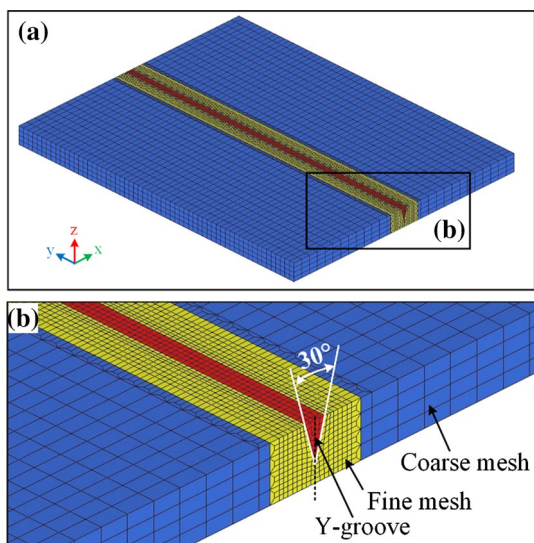


Fig. 5 Meshing of the sheet

4 Result

4.1 Weld Appearance and Microstructure

The morphology parameters of the laser-MIG hybrid welding joint given in Fig. 7. In the center of welded joint cross section, a fusion zone is observed and marked in Fig. 7a.

The influence of different welding parameters on macro morphology are shown in Fig. 7b, c. For case 3, 5 and 6, the welding velocity is the single variable. For case 2 and 6, the gas flow rate is the single variable. For case 3 and 4, the defocusing amount is the single variable.

It is found that the width (W) decreased with the increasing of welding velocity under the same laser power. The height (H) is biggest in case 5 with the welding velocity of 1.3 m/min. Comparative study of case 2 and 6 with different gas flow rate, case 6 has a bigger H and narrower W. The gas flow rate of 20L/min is benefit for the absorption of hybrid power under the same laser power of 3200 W and welding velocity of 1.5 m/min. Comparative study of case 3 and 4 with different defocusing amount, the case 3 with a more higher intensity of power gets a higher H', W and smaller root height (H₃) and concave deepness (H₁). The distance of fusion zone to the weld upper surface (H₂) is approximately 38%-47% of H.

The welding heat input is a significant parameter to evaluate the welding. The welding heat input of laser beam and MIG are calculated by the below energy input equations [23].

$$Q_{laser} = P/v \tag{7}$$

$$Q_{MIG} = UI/v \tag{8}$$

$$Q = Q_{laser} + Q_{MIG} \tag{9}$$

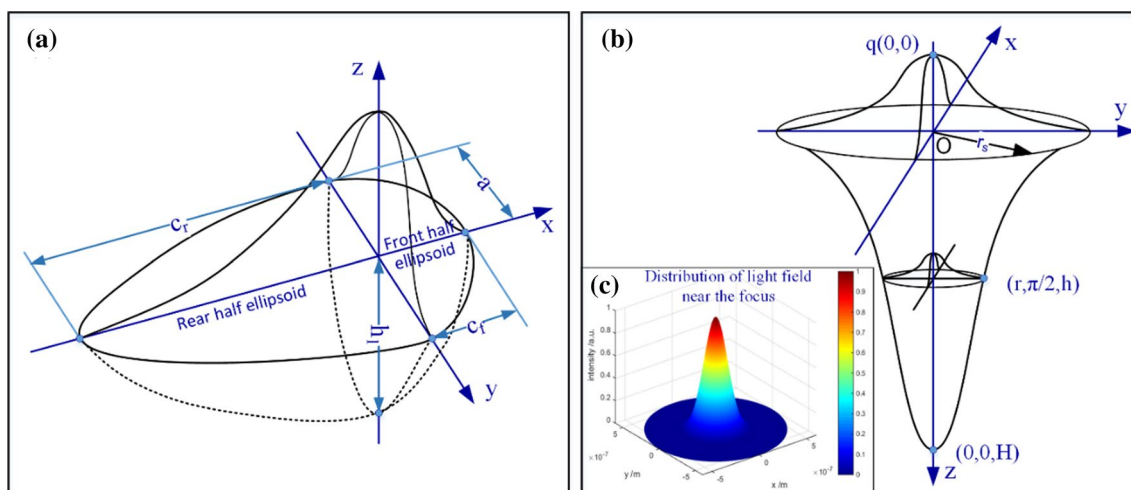


Fig. 6 Heat source model. a The double-ellipsoid (MIG) heat source model. b The Gaussian rotator (Laser beam) heat source model. c Distribution of light field near the laser focus

Table 4 Material properties of 5A06 aluminum alloy

| Materials properties | Temperature (°C) | | | | | | |
|---|------------------|-----|------|------|------|------|------|
| | 20 | 100 | 200 | 300 | 400 | 500 | 630 |
| Thermal conductivity (W m ⁻¹ K ⁻¹) | 118 | 121 | 126 | 130 | 138 | 140 | 140 |
| Specific heat (J kg ⁻¹ K ⁻¹) | 898 | 951 | 1003 | 1047 | 1080 | 1150 | 1165 |



Fig. 7 The influence of welding parameter on macro morphology **a** Morphology parameters of the laser-MIG hybrid welding joint. **b** The influence of welding velocity on macro morphology. **c** The influence

of gas flow rate on macro morphology. **d** The influence of defocusing amount on macro morphology

Table 5 Measurement results of laser-MIG hybrid weld specimens with the different parameters

| Case | Q_{laser} (J/mm) | Q_{MIG} (J/mm) | Q (J/mm) | H (mm) | W (mm) | H_1 (mm) | H_2 (mm) | H_3 (mm) |
|------|--------------------|--------------------|--------------------|--------|--------|------------|------------|------------|
| 1 | 1.4×10^5 | 0.88×10^5 | 2.28×10^5 | 9.71 | 8.08 | -1.27 | 3.72 | 2.81 |
| 2 | 1.28×10^5 | 1.37×10^5 | 2.65×10^5 | 7.91 | 9.67 | -0.93 | 3.62 | 1.01 |
| 3 | 1.6×10^5 | 1.72×10^5 | 3.32×10^5 | 9.88 | 9.38 | -1.06 | 3.86 | 2.98 |
| 4 | 1.6×10^5 | 1.72×10^5 | 3.32×10^5 | 8.44 | 10.63 | -0.53 | 3.69 | 1.54 |
| 5 | 1.48×10^5 | 1.58×10^5 | 3.04×10^5 | 10.76 | 9.05 | -1.93 | 5.04 | 3.86 |
| 6 | 1.28×10^5 | 1.37×10^5 | 2.65×10^5 | 9.77 | 8.92 | -1.07 | 4.09 | 2.87 |

where Q_{laser} is the heat input of laser beam, Q_{MIG} is the heat input of MIG, Q is the heat input of laser-MIG hybrid welding, P is the laser power, v is the welding velocity, U is the MIG voltage, I is the MIG current.

In Table 5, the calculated heat input and the measured value are presented. The maximum H , H_2 and H_3 are

achieved under the Q of 3.04×10^5 J/mm. It confirmed that the laser-MIG hybrid welding heat input absorptivity of BM is highest under case 5. The maximum W is achieved under the maximum Q_{MIG} of 1.72×10^5 J/mm.

The weld appearance and microstructure of case 6 are shown in Fig. 8, where the heat affected zone (HAZ), WS,

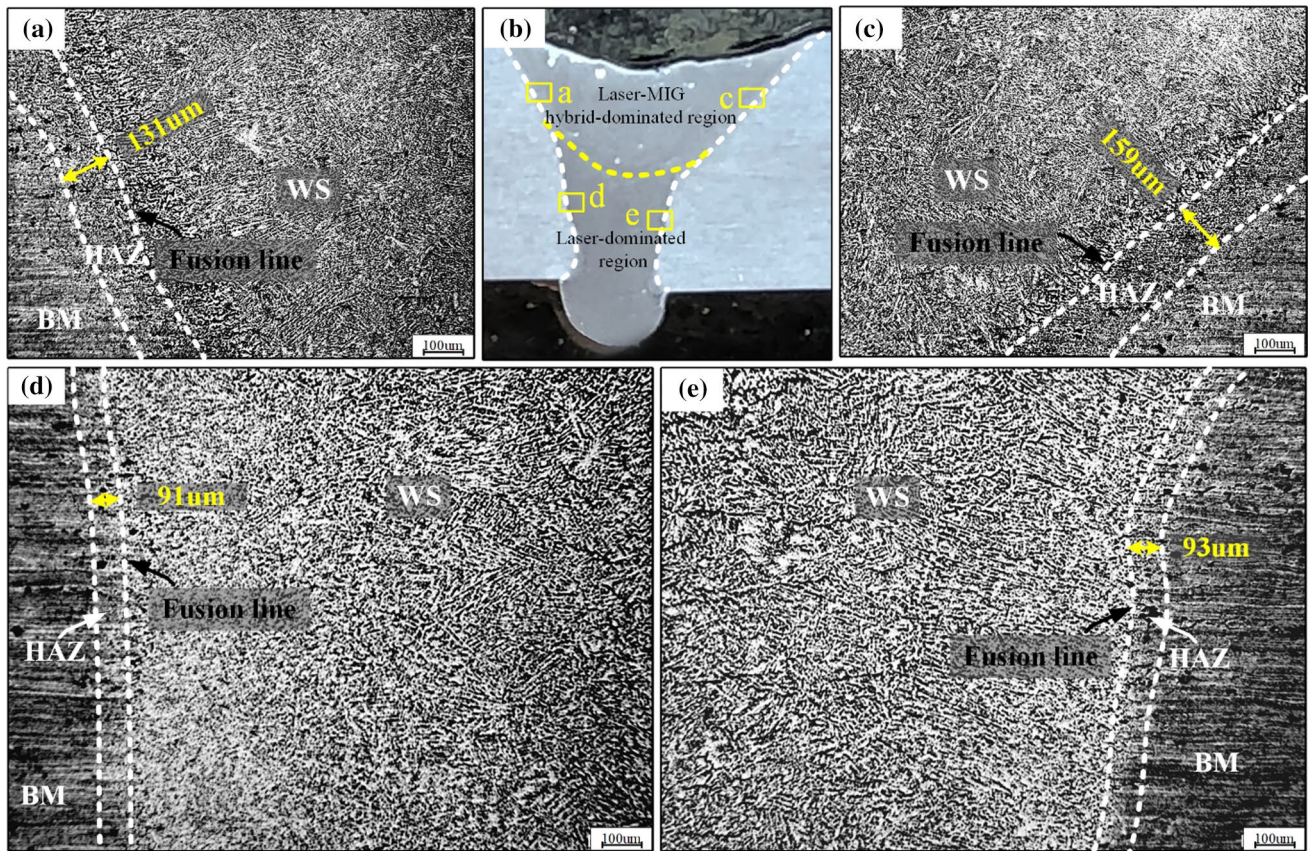


Fig. 8 Laser-MIG hybrid weld appearance and microstructure of case 6. **a** and **c** Vicinity of fusion line in the laser-arc hybrid dominated region. **b** Weld appearance. **d** and **e** Vicinity of fusion line in the laser-dominated region

BM, dendrite grain, and fusion line are marked. In the laser-MIG hybrid welding pool, the temperature gradient and crystallization rate in different parts are various, which leads to different weld morphology and crystal structure. From the fusion line to WS, the grain morphology is gradual transitioned from columnar grains to equiaxed dendrite grains. The specific widths of HAZ in different weld region are measured and marked in Fig. 8a, c–e. It is clearly observed that the HAZ in the upper area is wider than the bottom area of the welded joint. Besides, the width and volume of laser-MIG hybrid-dominated region are bigger than the laser-dominated rejoin. Under the same welding velocity, the bigger volume of weld pool has a lower cooling rate. The different width of HAZ is depends on the different width and volume of laser-MIG hybrid-dominated and laser-dominated rejoin.

It might also be noted that the second fusion line is observed in the center area of the welded joint as shown as Fig. 9c–e, which is marked by dashed yellow. The laser-MIG hybrid-dominated region is upon the second fusion line and the laser-dominated region is below the second fusion line. In the WS, the dendrite is formed. The crystalline size of equiaxed dendrite grains in the region upon the second

fusion line is finer than the region below the second fusion line.

Generally, crystalline size is expressed by the number of grains per unit volume (Z), Z is determined by the nucleation rate (N) and growth speed (u). The relationship of Z , N , and u is shown in the Eq. (7).

$$Z = 0.9(N/u)^{3/4} \quad (7)$$

Crystalline size is decreased with the increasing of N , while increased with u . During solidification, N and u are increased with the degree of under cooling. Besides, N is increased much faster than u . In other words, with the increasing of degree of under cooling, N/u is increased. Thus, Z is increased and the crystalline size is finer.

With the laser-arc distance of 3 mm, the laser beam firstly works on the welding metal. Under the action of laser beam, 5A06 aluminum alloy is violently vaporized and the molten material is rushed out under the generated pressure to form the weld keyhole. The laser beam is reflected and absorbed repeatedly by the wall of keyhole to increase the depth of keyhole. At the same time, the weld pool is formed. After 0.12–0.15 s, the electric arc is worked on the molten pool. Therefore, the bottom area of the WS is regard

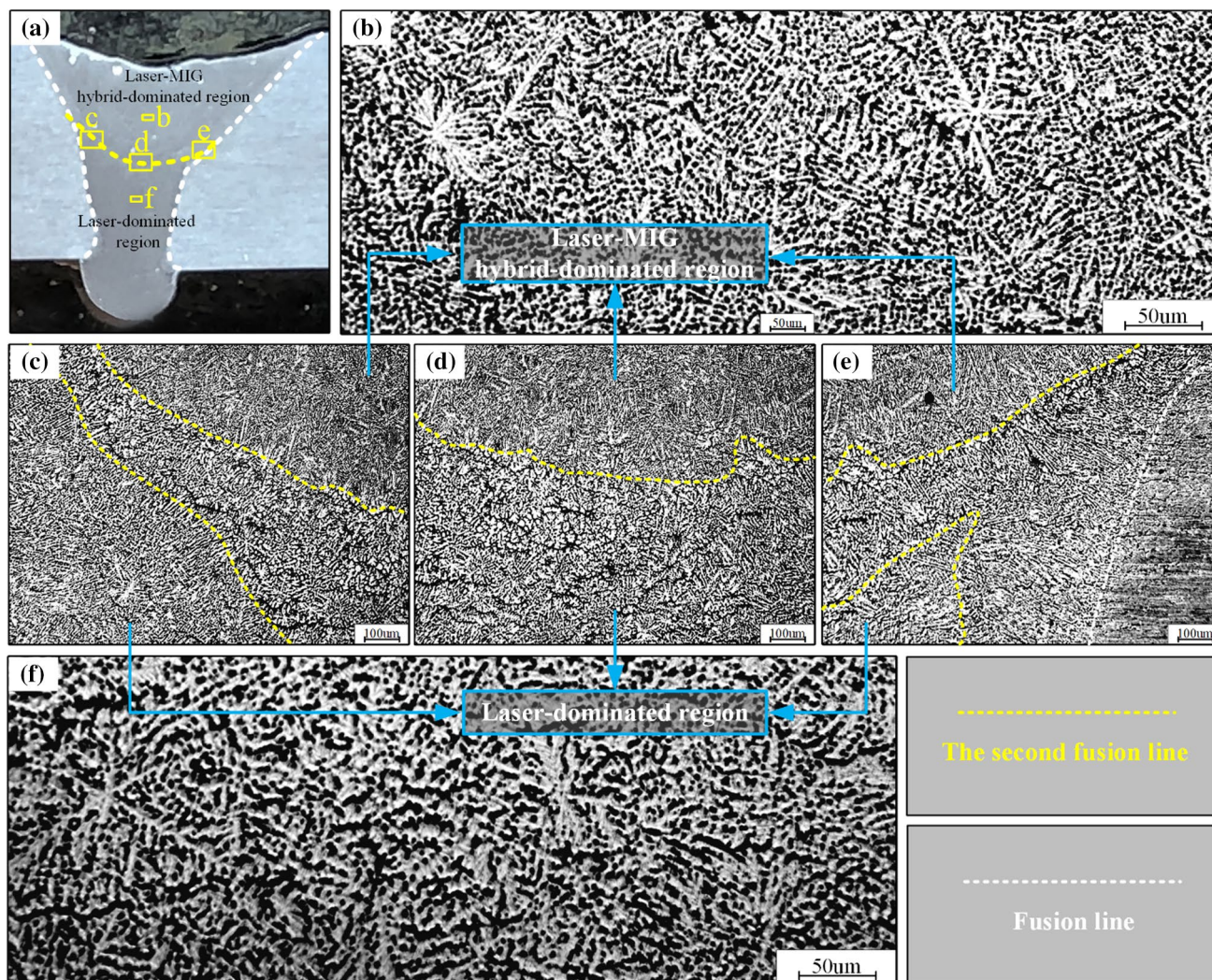


Fig. 9 Laser-MIG hybrid weld appearance and microstructure of case 6. **a** Weld appearance. **b** Fine dendrite in the laser-arc hybrid-dominated region. **c**, **d** and **e** Vicinity of the second fusion line between

the laser-arc hybrid-dominated region and laser-dominated region. **f** Coarse dendrite in the laser-dominated region

as single laser-dominated region, while the upper area is laser-arc hybrid-dominated region. The formation mechanism of laser-MIG hybrid-dominated region and single laser-dominated region are shown in Fig. 3. The heat input of laser-arc hybrid-dominated region is much higher than the laser-dominated region owing to the synergetic affects of the laser beam and MIG. In other words, the degree of under cooling of laser-arc hybrid-dominated region is much higher than the laser-dominated region. Thus, the crystalline size of equiaxed dendrite grains in the laser-MIG hybrid-dominated region is finer than the laser-dominated region. The first formation of single laser-dominated region has a preheat effect on the laser-arc hybrid dominated region.

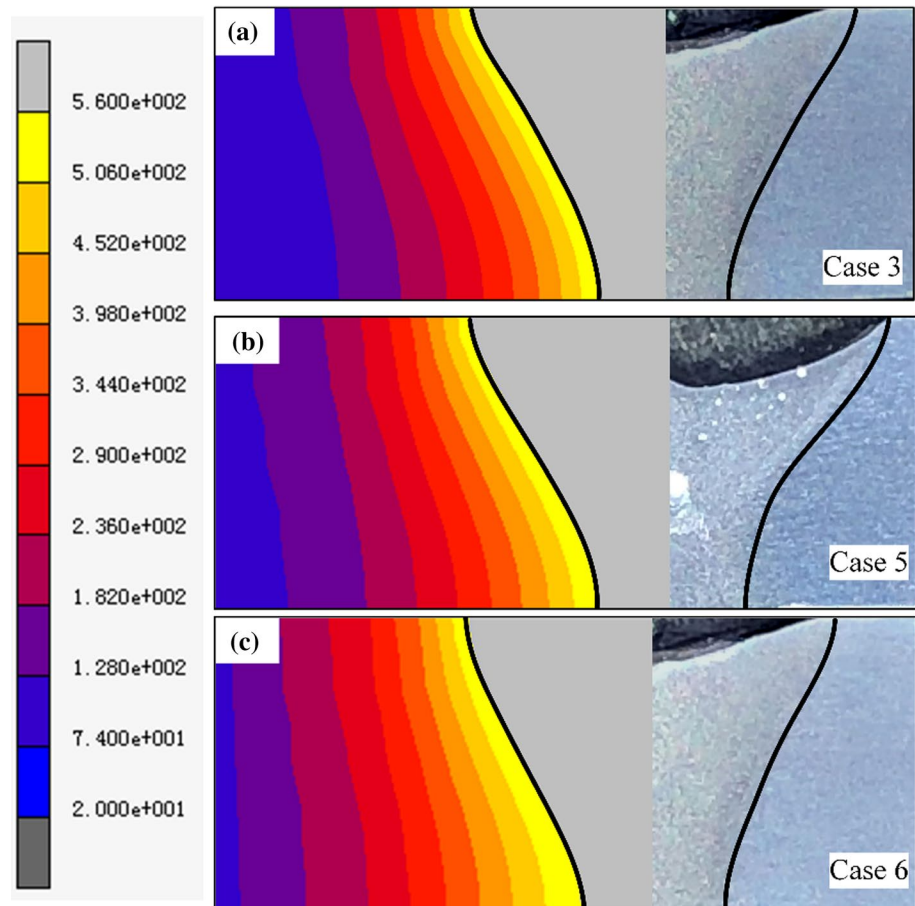
Conclusively, the formation of the HAZ with different width in the welded joint, the formation of the second fusion line and the formation of different size of equiaxed dendrite

grains in the welded joint are mainly owing to the different heat effect of laser-arc hybrid-dominated region and laser-dominated region.

4.2 Numerical Analysis Results

In the process of laser-MIG hybrid welding, the energy loss involves the reflectivity of the material, the power consumption of the machine, and the interactions between shielding gas and energy beam. The power transmitted to the material and converted into heat is lower than that produced by the laser beam and arc. Therefore, a calibration of the numerical model should be conducted. Figure 10 shows the contrast effects of actual WS cross sections obtained in the welding experiments and simulated temperature distributions from the finite element model. As shown in Fig. 10, the

Fig. 10 Calibration of the numerical model by comparing the cross section of the specimen and the cross section achieved through the numerical analysis of **a** case 3, **b** case 5, and **c** case 6



temperature of the weld pool is much higher than the melting point $560\text{ }^{\circ}\text{C}$ which is displayed in gray. The simulation results approach the experimental results with a good agreement for laser-MIG hybrid welding. It is observed that the molten pool obtained in the numerical analysis shows the similar shape with those in welding experiment.

Every node in WS has gone through a fast melting and solidification operation. In the temperature field model, the laser-MIG hybrid welding process is divided into 2300 time steps for precise simulation. The simulation of the first 300 time steps are mainly under the effect of the laser-MIG hybrid heat source. The simulation of the next 2000 time steps are mainly under the cooling effect of the $20\text{ }^{\circ}\text{C}$ surrounding environment.

Three nodes in each specimen are evaluated. Figure 11b–d present the thermal cycle curves of different nodes of laser-MIG hybrid welding process. The temperature calculation result of node 3198 in the laser-MIG hybrid-dominated region, node 3193 in the center fusion zone, and node 3156 in the laser-dominated region are shown in Fig. 11a. The maximum values of temperature in the three nodes reach approximately $1700\text{ }^{\circ}\text{C}$, $1230\text{ }^{\circ}\text{C}$, and $900\text{ }^{\circ}\text{C}$, respectively. The temperature of node 3198 is much higher than node 3156. It is deduced that there is a large temperature

gradient from the node 3198 to node 3156 of the molten pool. According to the simulation result, it demonstrated that the temperature of laser-MIG dominated region is higher than the laser-dominated region. The different distribution of temperature also leads to the different size of equiaxed dendrite grains in the welded joint.

Furthermore, it only takes approximately 3 s cooling from the highest temperature to $300\text{ }^{\circ}\text{C}$ during laser-MIG hybrid welding process. There is a sharp gradient in every node during welding process. All of the temperature of node 3198 and node 3193 are higher than the boiling point of Mg element, $1105\text{ }^{\circ}\text{C}$. Therefore, it is inevitable that Mg element is easy to burn loss in this extremely high temperature process.

4.3 Tensile Property

The tensile property of 5A06 aluminum alloy joined by laser-MIG hybrid welding is lower than BM. In the welding process, the compressive stress firstly caused by thermal expansion during the melting stage. After that, the tensile stress is caused by cooling shrinkage during solidification stage. What's more, the microstructure of WS is changed. The tensile property is reduced directly owing to the transformation of microstructure and stress.

Fig. 11 **a** The position of the three selected nodes. **b** Thermal cycle curve of case 3. **c** Thermal cycle curve of case 5. **d** Thermal cycle curve of case 6

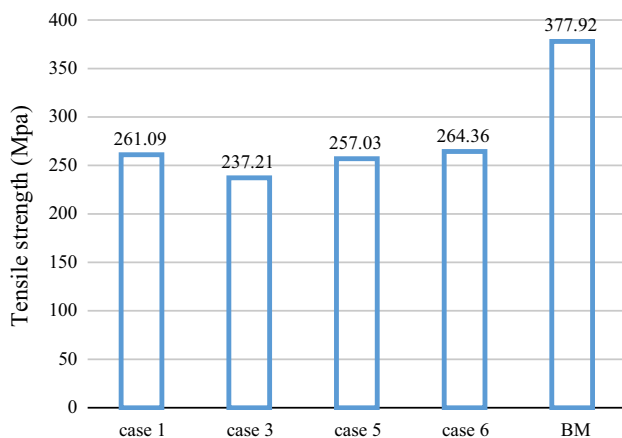
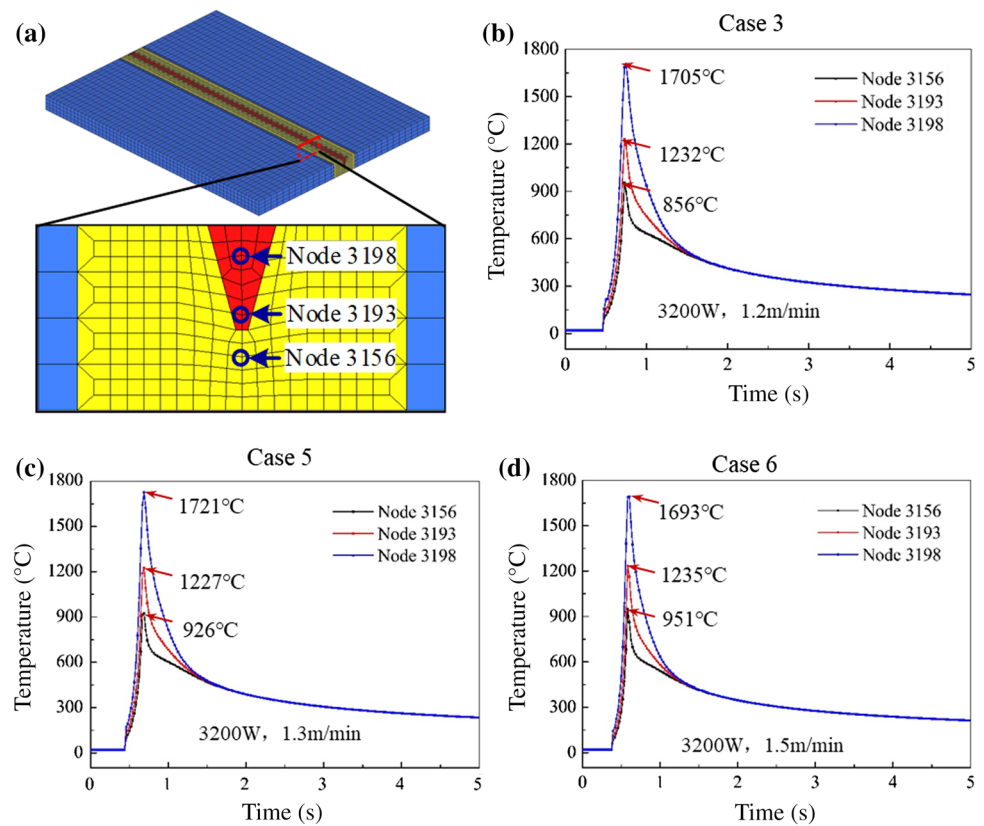


Fig. 12 Tensile strengths

Figure 12 shows the tensile strength for the butt joint of BM and weldment with different welding parameters. The tensile strength of BM is higher than the welded joints. The highest tensile strength of weldments reaches 263.36 MPa in the WS of case 6, 70% of the value of BM. Under static tensile loading, the fracture firstly appeared in laser-MIG hybrid-dominated region of WS. A slight plastic deformation and ductile fracture are appeared in the WS during tensile test.

The morphologies and element content of fractured tensile specimen are presented in Fig. 13. The fracture occurred at the center of the welded joint and the coarse pores are found at the fracture location. The coarse pores are mainly generated in the laser-MIG hybrid-dominated region. It has been found that the coarse pores have a great influence on the tensile properties of the weld. The existence of the coarse pores is the main factor for the fracture in the laser-MIG hybrid-dominated region where the fracture firstly appeared.

The element contents of BM, filling wire, and point 1–4 are shown in Table 6. In tensile fracture, the value of Mg(wt%)/Al(wt%) in point 1 is lower than BM and filling wire because the Mg element with a low boiling point of 1107 °C is extremely easy to vaporize during the high-energy density beam welding. Besides, the content of O and Mg element in point 2–4 at the position of coarse wall are higher than point 1 which is mainly owing to the formation of oxides. Both the Mg(wt%)/Al(wt%) of point 2 and 4 in grayish black are higher than BM and filling wire. The increasing of Mg element of point 2 and 4 are mainly owing to the formation of β phase Mg_2Al_3 . The β phase Mg_2Al_3 is dark gray. As a result, the corrosion resistance and the plasticity of the 5A06 aluminum alloy deteriorate. While point 3 has a lower content of O and Mg element, is light gray. The light gray in point 3 is mainly owing to the formation of the oxides i.e. Al_2O_3 , MgO. The formation of β phase Mg_2Al_3

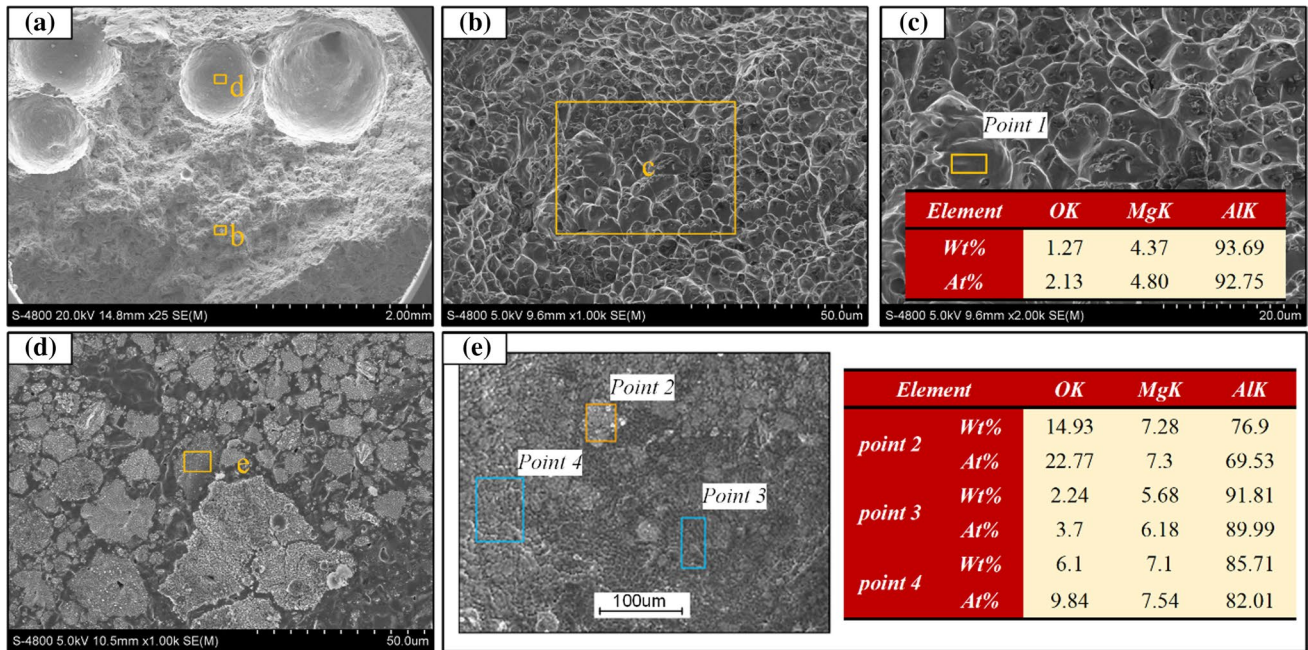


Fig. 13 Morphologies and element content of fractured tensile specimen. **a** Morphology of fractured tensile specimen. **b** Morphology of dimples. **c** Element content of dimple. **d** Morphology of pore wall. **e** Element content of pore wall

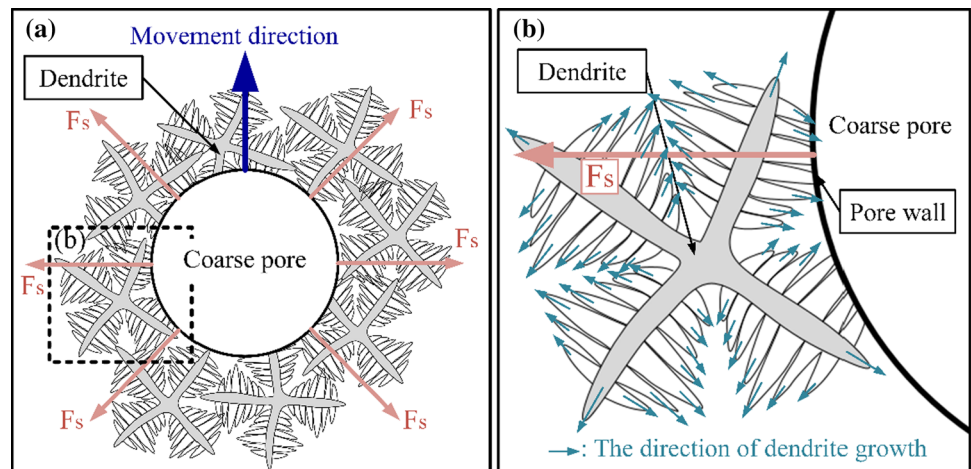
Table 6 The element contents of O, Mg and Al

| | O (wt%) | Mg (wt%) | Al (wt%) | $\frac{Mg (wt\%)}{Al (wt\%)} \times 100\%$ |
|--------------|---------|----------|----------|--|
| BM | 0 | 6.8 | 91.2 | 7.46% |
| Filling wire | 0 | 5 | 93.9 | 5.32% |
| Point 1 | 1.27 | 4.37 | 93.69 | 4.66% |
| Point 2 | 14.93 | 7.28 | 76.9 | 9.47% |
| Point 3 | 2.24 | 5.68 | 91.81 | 6.20% |
| Point 4 | 6.1 | 7.1 | 85.71 | 8.28% |

and oxides not only decrease the Mg and Al element content of substrate, but also easily assembled in the wall of pores during the solidification process.

As shown as Fig. 14, the finer equiaxed dendrite grains has connection of the coarse pores in the laser-MIG hybrid-dominated region. In the solidification process, the growth of equiaxed dendrite grains is hindered by the existence of coarse pore in the laser-MIG hybrid-dominated region. As shown as Fig. 14a, the pore wall has a surface tension (F_s) whose direction is along the normal direction of the wall.

Fig. 14 The growth of dendrite and pore



Some direction of dendrite growth is hindered by the pore wall.

5 Conclusion

In the current study, the laser-MIG hybrid welded joints for 6.9 mm thick 5A06 aluminum alloy with a laser-arc distance of 3 mm are researched. The second fusion line, laser-dominated region and laser-MIG hybrid-dominated region are introduced to explain the formation of different equiaxed dendrite grains in WS. The conclusions could be drawn as follows:

1. The degree of under cooling in laser-MIG hybrid-dominated region is much higher than the laser-dominated region. Thus, the crystalline size of equiaxed dendrite grains in the laser-MIG hybrid-dominated region is finer than the laser-dominated region. The first formation of single laser-dominated region has a preheat effect on the laser-MIG hybrid dominated region.
2. The formation of the second fusion line in the welded joint are mainly owing to the different heat effect of laser-arc hybrid-dominated region and laser-dominated region.
3. According to the simulation result, it observed that the molten pools obtained in the numerical analysis show the similar shape with those obtained in welding experiments. It demonstrated that the temperature of laser-MIG dominated region is higher than the laser-dominated region. The existence of temperature difference leads to the different size of equiaxed dendrite grains in the welded joint.
4. The highest tensile strength of welded joint reaches 263.36 MPa in the WS of case 6. The coarse pores are found at the fracture location. The element content of Mg and O in pore are higher than dimple. Besides, in the solidification process, the growth of equiaxed dendrite grains is in part hindered by the existence of coarse pores in the laser-MIG hybrid-dominated region.

Acknowledgement The authors gratefully acknowledge the financial support of the project from the State Key Lab of Digital Manufacturing Equipment & Technology (DMETKF2019010).

References

1. H. Yonetani, Laser-MIG hybrid welding to aluminum alloy carbody shell for railway vehicles. *Weld. Int.* **22**(10), 701–704 (2008)
2. T. Dursun, C. Soutis, Recent developments in advanced aircraft aluminum alloys. *Mater Design* **56**(4), 862–871 (2014)
3. J. Chen, Y. Wei, X. Zhan, P. Pan, Weld profile, microstructure, and mechanical property of laser-welded butt joints of 5A06 Al alloy with static magnetic field support. *Int. J. Adv. Manuf. Technol.* **92**(5–8), 1677–1686 (2017)
4. S.J. Kalita, Microstructure and corrosion properties of diode laser melted friction stir weld of aluminum alloy 2024 T351. *Appl. Surf. Sci.* **257**(9), 3985–3997 (2011)
5. S. Yan, Y. Nie, Z. Zhu, H. Chen, G. Gou, J. Yu, G. Wang, Characteristics of microstructure and fatigue resistance of hybrid fiber laser-MIG welded Al–Mg alloy joints. *Appl. Surf. Sci.* **298**(15), 12–18 (2014)
6. H. Jian, X. Tang, L. Ou, Y. Wang, Z. Yin, Interface Behavior of Aluminum Alloy by Multipass MIG Welding. *Rare Metal Mat Eng.* **45**(2), 415–420 (2016)
7. Y. Qi, J. Deng, Q. Hong, L. Zeng, Electron beam welding, laser beam welding and gas tungsten arc welding of titanium sheet. *Mater. Sci. Eng., A* **280**(1), 177–181 (2000)
8. Y. Yu, C. Wang, X. Hu, J. Wang, S. Yu, Porosity in fiber laser formation of 5A06 aluminum alloy. *J. Mech. Sci. Technol.* **24**(5), 1077–1082 (2010)
9. S. Toros, F. Ozturk, I. Kacar, Review of warm forming of aluminum–magnesium alloys. *J. Mater. Process. Technol.* **207**(1–3), 1–12 (2008)
10. T. Liang, L. Wang, Y. Liu, X. Song, Microstructure and mechanical properties of laser welded joints of dz125 l and in718 nickel base superalloys. *Met. Mater. Int.* **24**(3), 604–615 (2018)
11. I. Bunaziv, O.M. Akselsen, A. Salminen, A. Unt, Fiber laser-MIG hybrid welding of 5 mm 5083 aluminum alloy. *J. Mater. Process. Technol.* **233**, 107–114 (2016)
12. C. Gu, Y.H. Wei, X.H. Zhan, D. Zhang, S. Ren, H. Liu, H. Li, Investigation of welding parameters on microstructure and mechanical properties of laser beam-welded joint of 2060 Al–Cu–Li alloy. *Int. J. Adv. Manuf. Technol.* **91**(1–4), 1–10 (2016)
13. Z. Chen, Z. Hu, W. Lei, G. Ming, Z. Xiaoyan, Microcracking and mechanical properties in laser-arc hybrid welding of wrought al-6cu aluminum alloy. *Metall. Mater. Trans. A* **49**(10), 4441–4445 (2018)
14. P.S. Pao, S.J. Gill, C.R. Feng, K.K. Sankaran, Corrosion–fatigue crack growth in friction stir welded Al 7050. *Scripta Mater.* **45**(5), 605–612 (2001)
15. Z.H. Zhang, S.Y. Dong, Y.J. Wang, B.S. Xu, J.X. Fang, P. He, Microstructure characteristics of thick aluminum alloy plate joints welded by fiber laser. *Mater Design* **84**, 173–177 (2015)
16. W.M. Steen, Arc augmented laser processing of materials. *J. Appl. Phys.* **51**(11), 5636–5641 (1980)
17. C. Roepke, S. Liu, S. Kelly, Hybrid Laser Arc Welding Process Evaluation on DH36 and EH36 Steel. *Weld J* **89**(7), 140S–150S (2010)
18. X.H. Zhan, Q.Y. Gao, C. Gu, W. Sun, J.C. Chen, Y.H. Wei, The porosity formation mechanism in the laser-MIG hybrid welded joint of Invar alloy. *Opt. Laser Technol.* **95**, 86–93 (2017)
19. Ono M, Shinbo Y, Yoshitake A, Ohmura M (2002) Development of laser-arc hybrid welding. *Nkk Tech Rev* 70–74
20. J. Yan, M. Gao, G. Li, C. Zhang, X.Y. Zeng, M. Jiang, Microstructure and mechanical properties of laser-MIG hybrid welding of 1420 Al–Li alloy. *Int. J. Adv. Manuf. Technol.* **66**(9–12), 1467–1473 (2013)
21. J. Yan, X. Zeng, M. Gao, J. Lai, T.X. Lin, Effect of welding wires on microstructure and mechanical properties of 2A12 aluminum alloy in CO₂, laser-MIG hybrid welding. *Appl. Surf. Sci.* **55**, 7307–7313 (2009)
22. C. Li, K. Muneharua, S. Takao, H. Kouji, Fiber laser-GMA hybrid welding of commercially pure titanium. *Mater Design* **30**, 109–114 (2009)

23. Moradi M, Ghoreishi M, Khorram A (2018) process and outcome comparison between laser, Tungsten Inert Gas (TIG) and Laser-TIG Hybrid Welding. *Laser Eng* 39
24. M. Moradi, M. Ghoreishi, J. Frostevarg, A.F. Kaplan, An investigation on stability of laser hybrid arc welding. *Opt Laser Eng* **51**(4), 481–487 (2013)
25. S. Yan, H. Chen, Z. Zhu, G. Gou, Hybrid laser-Metal Inert Gas welding of Al–Mg–Si alloy joints: microstructure and mechanical properties. *Mater Design* **61**(9), 160–167 (2014)
26. G. Casalino, M. Mortello, P. Leo, K.Y. Bentounis, A.G. Olabi, Study on arc and laser powers in the hybrid welding of AA5754 Al-alloy. *Mater Design* **61**(9), 191–198 (2014)
27. P. Leo, G. Renna, G. Casalino, A.G. Olabi, Effect of power distribution on the weld quality during hybrid laser welding of an Al–Mg alloy. *Opt. Laser Technol.* **73**, 118–126 (2015)
28. M. Moradi, N. Salimi, M. Ghoreishi, H. Abdollahi, M. Shamsborhan, T. Ilar, A. Kaplan, Parameter dependencies in laser hybrid arc welding by design of experiments and by a mass balance. *J Laser Appl* **26**(2), 022004-1 (2014)
29. M. Moradi, M. Ghoreishi, A. Rahmani, Numerical and experimental study of geometrical dimensions on laser-TIG hybrid welding of stainless steel 1.4418. *J. Mod. Process. Manuf. Prod.* **5**(2), 21–31 (2016)
30. C. Zhang, M. Gao, D. Wang, J. Yin, X. Zeng, Relationship between pool characteristic and weld porosity in laser arc hybrid welding of AA6082 aluminum alloy. *J. Mater. Process. Technol.* **240**, 217–222 (2017)
31. Y. Meng, G. Li, M. Gao, X. Zeng, Effects of groove parameters on space constraint of narrow gap laser-arc hybrid welding. *J. Manuf. Process.* **33**, 144–149 (2018)
32. C. Cai, S. He, H. Chen, W. Zhang, The influences of Ar–He shielding gas mixture on welding characteristics of fiber laser-MIG hybrid welding of aluminum alloy. *Opt. Laser Technol.* **113**, 37–45 (2019)
33. X. Zhan, Y. Liu, W. Ou, C. Gu, Y. Wei, The numerical and experimental investigation of the multi-layer laser-MIG hybrid welding for Fe36Ni invar alloy. *J. Mater. Eng. Perform.* **24**(12), 4948–4957 (2015)
34. Z. Zeng, X. Wu, M. Yang, B. Peng, Welding distortion prediction in 5A06 aluminum alloy complex structure via inherent strain method. *Open Access Metall J* **6**(9), 214 (2016)

Publisher's Note Springer Nature remains neutral with regard to jurisdictional claims in published maps and institutional affiliations.